

A molecule-rich torus-like structure in the 21 μm source IRAS 23304+6147

Hao-Min Sun¹, Yong Zhang^{1,2,3*}, Xu-Jia Ouyang¹, Sheng-Li Qin⁴, Junichi Nakashima^{1,3}, Jian-Jie Qiu⁵, and Xiao-Hu Li^{2,6,7}

¹ School of Physics and Astronomy, Sun Yat-sen University, 2 Daxue Road, Tangjia, Zhuhai 519082, Guangdong Province, China
e-mail: zhangyong5@email.sysu.edu.cn

² Xinjiang Astronomical Observatory, Chinese Academy of Sciences, 150 Science 1-Street, Urumqi 830011, China

³ CSST Science Center for the Guangdong-Hongkong-Macau Greater Bay Area, Sun Yat-Sen University, Guangdong Province, China

⁴ School of physics and astronomy, Yunnan University, Kunming 650091, China

⁵ School of Mathematics and Physics, Jinggangshan University, 28 Xueyuan Road, Qingyuan District, Ji'an 343009, Jiangxi Province, China

⁶ Xinjiang Key Laboratory of Radio Astrophysics, 150 Science 1-Street, Urumqi, Xinjiang 830011, China

⁷ Key Laboratory of Radio Astronomy and Technology, Chinese Academy of Sciences, A20 Datun Road, Chaoyang District, Beijing, 100101, China

March 18, 2025

ABSTRACT

Context. A long-standing enigma in observational astronomy is the identification of the so-called 21 μm feature in a subset of envelopes of post-asymptotic giant branch (post-AGB) stars. Identifying this transient feature is important for understanding the chemical processes during the brief post-AGB phase and the enrichment of the interstellar medium. Understanding the structures and chemical environments of these objects is a prerequisite for such an endeavor.

Aims. We investigate the structure of the circumstellar envelope and the spatial distribution of gas-phase molecules in the 21 μm source IRAS 23304+6147, aiming to explore the potential physicochemical conditions required for the emergence of the 21 μm feature.

Methods. Molecular line observations toward IRAS 23304+6147 at the 1.3 mm band were performed using the Northern Extended Millimeter Array. A morpho-kinematic model was built to reproduce the observed ^{13}CO images and to decipher the structures of the nebula.

Results. The imaging results reveal an elliptically elongated shell with an equatorial density enhancement (or a torus-like structure), and in detail how the various molecules distribute in the envelope. The nebular morphology points to a binary system in which the ultraviolet radiation from the companion may trigger photochemistry in the inner regions. The torus-like structure exhibits an enrichment of linear carbon-chain molecules and a depletion of silicon-bearing molecules. This PPN has a mass lower limit of $1.3 \times 10^{-2} M_{\odot}$ and may exhibit a low $^{12}\text{CO}/^{13}\text{CO}$ abundance ratio.

Conclusions. The chemically stratified structure of ^{13}CN , HC_3N , and C_4H represents an observational evidence of the internal radiation that initiates photochemistry. The carbon-rich torus-like structure probably offers a conducive environment for the formation of dust and complex molecules implicated in the rare 21 μm emission. We hypothesize that the 21 μm sources probably descend from J-type carbon stars via a binary evolutionary channel.

Key words. Astrochemistry – Circumstellar matter – 21 μm source – Protoplanetary nebulae – Radio interferometer

1. Introduction

When low- and intermediate-mass stars evolve into the asymptotic giant branch (AGB) stage, intense stellar winds emanate from the stellar surface, propelling the circumstellar material into interstellar space at mass-loss rates typically ranging from 10^{-8} – $10^{-5} M_{\odot} \text{ yr}^{-1}$ and reaching as high as $10^{-4} M_{\odot} \text{ yr}^{-1}$ (e.g. Vassiliadis & Wood 1993; Bloeker 1995; Decin et al. 2019). The highly opaque AGB envelope is an enormous chemical factory (e.g., Cernicharo et al. 2000), where over 100 gas-phase molecules and 15 solid-state species have been detected (Decin 2021). After the high-mass loss ceases, the circumstellar material is gradually detached from the photosphere and the stellar temperature increases. Before the stellar ultraviolet (UV) radiation becomes intense enough to ionize the envelope, there is a

brief post-AGB phase, during which the star is surrounded by a protoplanetary nebula (PPN). The PPN stage lasts approximately 10^3 years. In contrast to the AGB envelope, whose morphology is predominantly spherical, the PPN's shape starts to deviate from overall spherical symmetry, becoming more complex (e.g., Sahai & Trauger 1998).

Recently, high angular resolution observations have revealed various structures in AGB envelopes, which may be attributed to the interaction of a companion (Boffin et al. 2012; Decin et al. 2020). The binary system plays an important role in the shaping of PPNe during the transition from AGB to post-AGB (see Lagadec 2018, for a review).

Apart from the morphology transition, PPNe show a chemical complexity. It is well established that circumstellar chemistry is determined by the C/O abundance ratio as the less abundant element is mostly locked up in CO. Carbon-rich cir-

* zhangyong5@email.sysu.edu.cn

cumstellar envelopes are dominated by carbonaceous molecules such as CS, CN, HCN, and HC₃N (e.g., Olofsson et al. 1993), whereas oxygen-rich envelopes predominantly contain oxygenated species like SO, OH, SO₂, and H₂O (e.g., Engels 1979). A large variety of gas-phase molecules have been detected in the prototype carbon-rich PPNe CRL 2688 and CRL 618 through spectral line surveys with single-dish telescopes (Pardo et al. 2007; Park et al. 2008; Zhang et al. 2013; Qiu et al. 2022). There is ample observational evidence showing that aromatic and aliphatic materials as well as C₆₀ can be quickly synthesized in the PPN phase (Kwok et al. 2001; Zhang & Kwok 2011).

A quintessential example of the chemical complexity in PPNe is the discovery of the 21 μ m feature. This feature was discovered for the first time by Kwok et al. (1989), and has been detected so far in only 31 objects (20 in the Galaxy, 9 in the Large Magellanic Cloud, and 2 in the Small Magellanic Cloud; see Volk et al. 2020, for a recent review). All the 21 μ m sources are carbon-rich PPNe with largely enriched *s*-process elements (van Winckel 2003). The rare detection indicates a transient nature. Observations show that the 21 μ m feature is always accompanied by a broad feature at 30 μ m, with the former accounting for about 1%–5% of the infrared emission of the PPN, and the latter accounting for about 7%–20% (Zhang et al. 2010); but there is no correlation between the intensities of the two features (Jiang et al. 2010). The 21 μ m feature remains unidentified although a dozen different species, ranging from individual carbon- or silicon-bearing molecules to polycyclic aromatic hydrocarbon complexes, have been proposed as the potential carriers (see the references in Volk et al. 2020). Some of them can be ruled out because of the insufficient cosmic abundance of the incorporated elements or the non-detection of sub-features arising from the same species (Zhang et al. 2009). It is unclear why this feature abruptly appears and rapidly disappears and what role its carrier could play on circumstellar chemistry. Unraveling its origin is crucial to deepening our understanding of the enrichment of the interstellar medium.

The exclusive presence of the 21 μ m feature in carbon-rich PPN suggests a significant link to carbon-chain chemistry. It follows that investigating carbon-bearing molecules within 21 μ m sources could reveal critical insights into the identification of this mysterious feature (Zhang 2020; Qiu et al. 2024). However, the scarcity of 21 μ m sources, the inherent faintness of molecular lines in these sources, and our incomplete understanding of circumstellar chemistry during the brief PPN period present significant challenges to this research. As a crucial first step of investigating the physicochemical environments necessary for the formation of the 21 μ m carrier, we need to perform high-sensitivity observations and statistically study the nebular characteristics that are common for the 21 μ m sources. Previous efforts have been mostly based on single-dish observations although interferometric observations of CO emission in a few 21 μ m sources have been presented (Nakashima et al. 2009, 2012; Ueta et al. 2019), which are unable to reveal the chemical complexity induced by the morphology evolution of PPNe.

In this paper, we present millimeter interferometry observations of a prototypical 21 μ m source IRAS 23304+6147, aiming to investigate the nebular structure and the spatial distributions of the gas-phase molecules. The observations and data reduction are described in Section 2. The spectra and images of the identified molecules are presented in Section 3, along with a morphokinematic model that is developed to explain the data. In Section 4 we discuss the nature and origin of the nebular structure,

the ¹²CO/¹³CO abundance ratio, and the implications on circumstellar chemistry. Our conclusions follow in Section 5.

2. Observation and Data Reduction

IRAS 23304+6147 was observed utilizing the Northern Extended Millimeter Array (NOEMA) Interferometer in configuration 12A on 2022 February 23 (1.9 h on source), February 28 (2.9 h on source), and March 6 (0.8 h on source) under the project number W21BI (PI: Y. Zhang). The precipitable water vapor during the observations spreads over 0.4–1.2 mm. The system temperatures range from 100–150 K. Twelve antennas were using with baselines ranging from 32–920 m. The observations were performed with the lower sideband (LSB) covering 213–221 GHz and the upper sideband (USB) covering 228–236 GHz. Doppler tracking was employed, establishing a central velocity of -16.1 km s^{-1} , the systematic velocity of IRAS 23304+6147, relative to the local standard of rest (LSR). The phase calibrators are 0059+581, J0011+707, and J2250+558; the bandpass calibrators are 0059+581 and 3C84. MWC349 and 2010+723 were observed for flux calibration, which have flux densities of 2.1 and 0.6 Jy, respectively.

The phase center was set at $(\alpha_{2000}, \delta_{2000}) = (23^{\text{h}}32^{\text{m}}44^{\text{s}}785, +62^{\circ}03'49.084'')$. Data were calibrated using the GILDAS/CLIC package¹. Imaging and deconvolution processes were conducted using GILDAS/MAPPING and GILDAS/IMAGER². The CLEAN algorithm of Högbom (1974) was employed in the imaging process. Uniform weighting was used in order to optimize the spatial resolution, resulting in a synthesized beam of $0.52'' \times 0.42''$ at a position angle (PA) of 23° . Molecular maps were obtained by subtracting the maps of continuum emission extracted from line-free spectral channels. The Root-mean-square (rms) noise of the line channel maps is $1.25\text{--}1.61 \text{ mJy beam}^{-1}$. The spectral resolution is about 2 MHz (2.7 km s^{-1}) at 1.3 mm.

3. Results

3.1. Spectral lines

Previously reported single-dish observations toward IRAS 23304+6147 have detected CO ($J = 1\text{--}0$ and $2\text{--}1$) (Woodsworth et al. 1990; Likkell et al. 1991; Hrivnak & Bieging 2005), ¹³CO ($J = 1\text{--}0$ and $2\text{--}1$) (Sánchez Contreras & Sahai 2012; Qiu et al. 2024), CS ($J = 3\text{--}2$) (Omout et al. 1993), HCN ($J = 1\text{--}0$ and $3\text{--}2$), H¹³CN ($J = 3\text{--}2$), and CN ($N = 2\text{--}1$) (Qiu et al. 2024). Our interferometric observations result in detections of 17 individual emission features belonging to eight different molecules and isotopologues, among which C¹⁸O, ¹³CN, HC₃N, C₄H, SiS, and SiC₂ are observed for the first time in this source. Figure 1 shows the spectrum obtained by averaging the flux densities over a $2'' \times 2''$ area centered on the phase center. Line measurements are presented in Table 1, where E_u is the energy of the upper level, and I_{peak} and $\int I dv$ represent the peak and integrated intensities, respectively. The line profiles are shown in Figure 2, where the flux density has been converted to Jy using a conversion factor of approximately 32.8 Jy/K.

In order to estimate the flux loss of our NOEMA observations, we compare the single-dish data of the CO and ¹³CO ($J = 2\text{--}1$) lines observed by the Heinrich Hertz Sub-millimeter

¹ <http://www.iram.fr/IRAMFR/GILDAS>

² <https://imager.oas.u-bordeaux.fr>

Telescope (HHT) and the 10m Arizona Radio Observatory Submillimeter Telescope (SMT), respectively (Hrivnak & Bieging 2005; Qiu et al. 2024). Figure 3 shows a comparison of the ^{13}CO ($J = 2-1$) observations made by NOEMA and SMT. According to the single-dish observations, the CO and ^{13}CO lines have peak intensities of 0.2 and 0.025 K and integrated intensities of 3 and 0.33 K km s^{-1} , respectively. The half-power beamwidths (HPBW) of HHT and SMT are $32''$ at 230 GHz and $34.3''$ at 220 GHz, respectively. According to the NOEMA images, the source size is roughly $2''$, resulting in filling factors of 0.0039 and 0.0034 for the HHT and SMT beams, respectively. If there is no flux loss, the CO and ^{13}CO lines should have peak intensities of 90 and 12 mK and integrated intensities of 0.93 and 0.12 K km s^{-1} in the HHT and SMT observations, respectively. This indicates a flux loss of 70% in our NOEMA CO and ^{13}CO line observations. Extended fossil AGB halos have been revealed in other PPNe (e.g., Sahai et al. 2007). It is likely that an AGB halo has been substantially filtered out in our observations. Presumably, the flux loss is less severe for other lines that have a spatial extension significantly smaller than CO.

3.2. Maps

Figure 4 shows the maps of continuum emission at 1.39 and 1.28 mm, which have flux densities of 3.67 and 3.57 mJy, respectively, indicating an in-band spectral index³ of $\alpha = -0.3$. The derived α value appears to be in close proximity to the theoretical predictions of optically thin free-free emission (-0.1). However, since the central star of this PPN lacks sufficient ionizing flux to sustain extended ionized regions, the physical origin of the spectral index remains unclear. Owing to the restricted frequency range and feeble continuum emission, we exercise caution and refrain from over-interpreting the result.

Figure 5 shows the continuum-subtracted moment 0 maps of molecular lines. Overall, the post-AGB nebula appears as an elongated ellipsoid (EE) with an equatorial density enhancement (EDE). The presence of the EE structure is consistent with previous optical observations (Sahai et al. 2007) and is typical of nascent PPNe (Bujarrabal et al. 1992). The NOEMA maps show that different molecules have notably different spatial distributions, demonstrating a significant chemical stratification. The optically thick CO emission shows an oval-shaped structure with an inner bright ring and an outer halo. The EDE structure is more striking in the ^{13}CO map, and manifest itself as a torus-like structure in the maps of linear carbon-chain molecules (C_4H and HC_3N). It should be noted that the gaseous torus-like structure has also been detected in other $21\text{ }\mu\text{m}$ sources IRAS 07134+1005, IRAS 22272+5435, and IRAS 16594-4656 (Nakashima et al. 2009, 2012; Ueta et al. 2019). Despite their very modest emission, silicon-bearing molecules (SiS and SiC_2) seem to be distributed in the peripheral regions of the envelope with fragmentary structures. Intriguingly, the SiS and SiC_2 fragments do not coincide in position. The ^{13}CN emission is dominantly concentrated in the center, while the C^{18}O emission is too faint to draw any conclusion about its spatial distribution.

The channel maps of CO, ^{13}CO , and HC_3N lines are shown in Figures 6–8. An inspection of these maps reveals that the intensity distributions highly depend on the velocities. In the red channels ($V_{\text{LSR}} > -3\text{ km s}^{-1}$) the EE appears as a bright spot located in the northwest region, while in the blue channels

($V_{\text{LSR}} < -29\text{ km s}^{-1}$) the bright region of EE is shifted to the southeast. The behavior of the EDE in the channel maps is opposite to that of the EE. As seen in the channel maps of ^{13}CO and HC_3N (Figures 7 and 8), the crescent-shaped EDE emission is shifted from the southeast to the northwest from the red to the blue channels ($V_{\text{LSR}} = -8$ to -27 km s^{-1}). This is a clear demonstration showing that the major axis of the EE is inclined toward us in the southeast, and the EE expands along the major axis faster than the EDE⁴.

3.3. Morpho-kinematic model

To investigate the structures of IRAS 23304+6147, we employ the three-dimensional morpho-kinematic modelling code SHAPE (Steffen & Koning 2012). We first input the initial parameters into SHAPE. Subsequently, through an iterative procedure, we generate synthetic images as well as position-velocity (P-V) diagrams that closely resemble the observational data. From the free parameters refined during this iterative process, we proceed to deduce the morpho-kinematic structure of the model. This methodology has been previously demonstrated to be successful in reconstructing PPNe in other research works (e.g., Koning et al. 2011; Nakashima et al. 2012; Santander-García et al. 2015; Tafoya et al. 2019).

The model consists of two components corresponding to the EDE and EE, as shown in Figure 9. We assume that the EDE and the EE are symmetric in the azimuthal direction around the EE's major axis. In a cylindrical coordinate system, we set the major axis of the EE as z -axis. Then, we can describe the molecular density distributions using a formula with the variables z and r , where z represents the vertical displacement relative to the central star, and r represents the orthogonal distance to the z -axis. We assume that the molecular gas is confined within the meshes shown in Figure 9 and the densities of the EDE and the EE follow the formulas,

$$n_{\text{EDE}}(r) = n_1 e^{-\frac{(r-r_1)^2}{2\sigma_1^2}}, \quad (1)$$

and

$$n_{\text{EE}}(z) = n_2 e^{-\frac{z^2}{2\sigma_2^2}}, \quad (2)$$

A simple Hubble flow is adopted for the velocity fields of the EDE and EE. Specifically, the maxima velocity of the EE is 2.5 times that of the EDE.

Given the assumption that the ^{13}CO ($J = 2-1$) line is optically thin, which implies that its surface brightness is proportional to the ^{13}CO column density, we utilize the ^{13}CO channel maps to impose constraints on the density distribution and velocity fields within the model⁵. Figures 10 and 11 present the modeled channel maps and the residual maps, respectively. The optimized modelling parameters in Equation 1 and Equation 2 are as follows: $n_1 = 1.9 \times 10^7\text{ cm}^{-3}$, $r_1 = 2.8 \times 10^{16}\text{ cm}$, $\sigma_1 = 4.6 \times 10^{15}\text{ cm}$, $n_2 = 5.4 \times 10^6\text{ cm}^{-3}$, and $\sigma_2 = 2.2 \times 10^{16}\text{ cm}$.

⁴ The EE expands at different velocities along different directions, and has the highest velocity along the major axis, which is referred to the velocity of the EE hereafter for simplicity. The EDE expands along the equatorial direction at a constant velocity.

⁵ The ^{13}CO ($J = 2-1$) line may not be optically thin in PPNe. For instance, Bujarrabal et al. (2013) show that the Red Rectangle's core is optically thick in ^{13}CO ($J = 2-1$) line. However, the morpho-kinematic reconstruction remains robust to slight deviations from the optically thin assumption.

³ The spectral index α is defined as the exponent in the power-law relation describing the dependence of the continuum flux density S_ν on frequency ν , given by $S_\nu \propto \nu^\alpha$.

The model successfully reproduces the main observable features of the primary nebula on the channel maps although it cannot precisely replicate the surface brightness. The existence of the EDE-EE structure is unequivocally corroborated, and the modeled velocities of the EDE and EE should be reliable. The model's performance deteriorates at the tip of the EE. In comparison to the observations, there is an displacement, which can be partially attributed to the oversimplified assumption of the density distribution and the photodissociation of ^{13}CO (see Section 4.2.3). Furthermore, as illustrated in Figure 11, approximately 20% of the total flux arises from a diffuse component not included in our current model. The diffuse emission exhibits remarkable intensity in the regions adjacent to the EDE and can be seen in all of the velocity channels where the EDE and EE are present. This extended emission can be attributed either to part of an AGB halo expanding at $\sim 20 \text{ km s}^{-1}$ or a disk-wind associated with the EDE.

Figure 12 shows a comparison between the observed P-V diagram and the modelling results. The kinetic structures of the EE and EDE are well traced by the P-V diagrams of ^{13}CO . We do not see signature of rotating disk that has been detected in a handful of PPNe (Gallardo Cava et al. 2021). The deduced inclination angles from the sky plane of the EDE and the EE are 35° and 55° , respectively. According to the modelling, the EE and EDE have maxima expansion velocities of about 35 and 14 km s^{-1} , respectively. The primary axis of the EE has an angular dimension of $2''$, whereas the inner and outer diameters of the EDE are $0.78''$ and $1.75''$. Adopting a distance of 4.32 kpc (Kamath et al. 2022), we estimate the inner and outer diameters of the EDE to be 3300 and 7500 AU and the EE primary axis to be 8600 AU in size. This results in dynamic ages of 340–770 yr and 600 yr for the EDE and EE, respectively. Consequently, we infer that the EE and EDE were formed approximately at the same time.

Although the values of the parameters used in the model are carefully chosen based on the observational data and our current understanding of stellar winds, we give no warranty that they represent the only possible solution. It is crucial to point out that the SHAPE modelling is intended to examine the morpho-kinematic structures of the nebula on relative scales. We have not carried out radiative transfer calculations in this model. Consequently, the results do not directly hinge on the temperature. In the future, it is highly desirable to develop a sophisticated radiative transfer model that incorporates ^{12}CO lines, which is more sensitive to the temperature, in order to achieve more precise results.

3.4. Nebular Mass

Once the excitation temperature is established, the mass of molecular gas (M) can be derived from the ^{13}CO ($J = 2-1$) line through the formula given by Olofsson & Nyman (1999) and Chiu et al. (2006). Drawing upon the approach delineated by Dinh-V-Trung (2009), we estimate the kinetic temperature (T_K) of the molecular gas to be approximately 10 K. Subsequently, we made use of the online radiative transfer modelling tool RADEX (van der Tak et al. 2007) to compute the excitation temperature of the ^{13}CO ($J = 2-1$) transition, which is roughly 10 K. Based on the same assumption for IRAS 08544–4431 (Dinh-V-Trung 2009), where $f_{13\text{CO}} = 2 \times 10^{-5}$, we find $M = 1.3 \times 10^{-2} M_\odot$ for the nebula around the post-AGB star IRAS 23304+6147. There are some uncertainties in calculating M . Regarding IRAS 08544–4431, the investigations carried out by Dinh-V-Trung (2009) and Bujarrabal et al. (2018) derived values of $M = 4.7 \times 10^{-3} M_\odot$ and $2.2 \times 10^{-2} M_\odot$, respectively. After

factoring in the effect of the different distances used in these calculations, this discrepancy indicates a five- to sixfold uncertainty in the mass estimation. Bujarrabal et al. (2018) implied a value of $f_{13\text{CO}} = 1.5 \times 10^{-5}$ for IRAS 08544–4431, which is comparable to the assumption made by Dinh-V-Trung (2009). However, their studies indicated that the disk temperature in IRAS 08544–4431 could potentially exceed 100 K. If we assume $T_K = 100 \text{ K}$, M will decrease by a factor of 1.5. Therefore, we estimate that the uncertainty in the calculated mass could be as large as a factor of eight. Because of flux loss, the derived M should be regarded as a lower limit to the nebular mass. There might be an extended AGB-remnant halo with a mass of $3 \times 10^{-2} M_\odot$.

4. Discussion

The NOEMA observations of IRAS 23304+6147 update the molecular richness of this source and offer new details about its nebular structure that was not disclosed by earlier optical measurements. In Section 4.1, we discuss the shaping of this PPN. In Section 4.2, we examine the connection between circumstellar chemistry and nebular structure, which may shed new light on the origin of the $21 \mu\text{m}$ feature.

4.1. Origin and nature of the EDE

As pointed out by Lagadec (2018), there are two types of EDEs. The first type is short-lived, created prior to the jet, and has a slow expansion velocity and limited angular momentum. One such example is that found in the water fountain IRAS 16342–3814 (Sahai et al. 2017). The second type is in Keplerian rotation with a large angular momentum, and has a longer lifetime. Disks of this kind commonly coexist with disk-winds, as demonstrated by observations of the PPNe AC Her and Red Rectangle (Bujarrabal et al. 2015, 2016). Observational studies (Gallardo Cava et al. 2021; Gallardo Cava 2023) have demonstrated that although these outflows generally exhibit lower mass budgets compared to their progenitor disks, they can occasionally exceed the mass of the rotating components they surround. Apart from the disk-winds, high-velocity jets may be generated from the companion star (Bollen et al. 2022). In contrast to disk-winds, these collimated high-velocity jets make only a negligible contribution to the overall nebular mass (Gallardo Cava 2023). As shown in Figure 12, the EDE of IRAS 23304+6147 has a slow expansion velocity of $\sim 20 \text{ km s}^{-1}$. For a Keplerian disk, the velocity should be inversely proportional to the radial distance from the center, however this is not the case in Figure 12. Therefore, the EDE does not exhibit rotation, and should be assigned in the first category. The formation of EDE is commonly attributed to the interaction in a binary system, where the mass loss from the primary star tends to be directed in the orbital plane in the gravitational field of the companion. A pre-existent circumbinary disk may slow down the super stellar winds along the equatorial direction, generating the EDE. Dynamic interaction could lead to an angular momentum transfer from the binary orbit to the EDE, forming an expanding torus structure. During further evolution the torus may feed a circumpanion accretion disk, leading to the launch of a jet (see Bollen et al. 2022, and reference therein).

Decin et al. (2020) show that in a binary system the favourable conditions for forming the EDE are large orbital eccentricity, low fraction of the stellar wind mass present within the orbital plane, large stellar mass, small orbital separation, and low mass-loss rate. Such conditions are often encountered in oxygen-rich stellar winds. Conversely, carbon-rich winds often

exhibit a spiral structure rather than EDE because of stronger acceleration by carbon-bearing dust (Decin et al. 2020). Therefore, the chance of detecting EDE in carbon-rich envelopes should not be large, although there exist such detections (e.g., Sánchez Contreras et al. 2004). However, our detection, together with those of Ueta et al. (2000) and Nakashima et al. (2009, 2012), suggest that the probability of 21 μm sources harbouring an EDE is high. Klochkova et al. (2000) posit that the overabundance of silicon in IRAS 23304+6147 may be caused by the hot bottom burning (HBB) process occurring in the hot layers of the convective envelope of a massive AGB star. This is a characteristic of J-type carbon stars (Chen et al. 2007), suggesting that the central star has an initial mass greater than $4 M_{\odot}$. According to the formula of Decin et al. (2020), the likelihood of developing an EDE structure would increase fivefold with a fourfold increase in stellar mass. Therefore, it is reasonable to infer that the formation of the 21 μm carrier might be associated to the short-lived EDE in massive carbon-rich PPNe. This could provide a plausible explanation for the low detection rate of this feature.

On the other hand, HBB predominantly consumes ^{18}O . De Nutte et al. (2017) show that the $^{17}\text{O}/^{18}\text{O}$ ratio is positively correlated with the initial mass of the post-AGB star. The $^{17}\text{O}/^{18}\text{O}$ ratio approximately equals to the ratio of integrated intensities of the C^{17}O and C^{18}O lines. We have detected the C^{18}O line; however, the C^{17}O line lies beneath our detection threshold. Consequently, the upper limit of the $^{17}\text{O}/^{18}\text{O}$ ratio is determined to be 0.5. In light of the relation presented by De Nutte et al. (2017), it can be inferred that the stellar initial mass is less than $1.5 M_{\odot}$. This inference implies that HBB does not play a significant role in this PPN, which stands in contrast to the conclusion drawn by Klochkova et al. (2000). We put forward the hypothesis that the discrepancy might be attributable to binary evolution, even though the specific details remain obscure.

The EDE has been also detected in the mid-infrared image of another 21 μm PPN IRAS 07134+1005 (Ueta et al. 2000; Kwok et al. 2002), which traces the dust emission. However, high-angular resolution CO and ^{13}CO maps show that it is a hollow shell with a slight velocity enhancement along the major axis, casting a doubt on the presence of the EDE (Ueta et al. 2019). If looking at the CO map along (Figure 6), we may have made the same claim for the morpho-kinematics of IRAS 23304+6147 that no EDE is seen. However, as clearly shown in Figure 5, carbon-chain molecules trace a torus-like structure. The CO map displays significantly different morphology mostly due to its optically thick nature. On the other hand, C_4H and HC_3N have subtly different spatial distributions with the former more concentrated in the torus, probably suggesting a chemical differentiation. From above discussion we can learn that PPNe's appearances have a molecule dependence. Utilizing the images of only one or two molecular lines may result in an unrealistic classification of nebular morphologies. Masa et al. (2024) provide compelling evidence for this molecular selectivity. Their interferometric observations demonstrate that HCO^+ and HCN maps resolve knotty structures spanning the central region to the polar tips of M1-92. Notably, these structures are absent in both the CO and ^{13}CO maps. Future observations with high spatial resolution could reveal the distribution of a wider range of molecules, not just CO, within the EDE and EE post-AGB structures.

4.2. Chemistry of the 21 μm PPN

The departure from spherical symmetry could result in spatially distinct chemical differentiation. The parent molecules ejected from the AGB star are ionized or dissociated by the UV pho-

tons from the external interstellar radiation field, which induces ion- or radical-neutral reactions, and thus increases the molecular complexity in the circumstellar envelope. As the star evolve into the PPN phase, the increasing temperature of the central star and the expansion of the envelope may strengthen the internal UV radiation, which in principle could also contribute to the photo and radiation chemistry of the envelope. State-of-the-art astrochemical models predict that under the assumption of a clumpy stellar wind and additional radiation from a hot companion, sufficient internal UV photons can penetrate deeply into the envelope and impose a significant influence on the circumstellar chemistry (Millar 2020; Van de Sande et al. 2023). Observational evidence for circumstellar chemistry driven by the internal UV radiation is still scarce. Different chemical processes in the EE and EDE may occur due to their different densities and extinctions that govern the penetration of the UV photons into the envelope. In the low-density EE, the collisions between molecules are relatively inefficient and the UV radiation is intense, and thus the synthesis of daughter molecules from photodissociation products is inefficient. The situation is contrary for the EDE, where the density is higher and daughter molecules can be synthesized more efficiently. With this in mind, the following subsections attempt to provide an interpretation of the spatial distribution of molecules in this PPN. In Sections 4.2.1 and 4.2.2, we discuss the carbon- and silicon-bearing molecules, respectively. Section 4.2.3 presents the spatial distribution of the $^{12}\text{CO}/^{13}\text{CO}$ ratio.

4.2.1. Carbon-bearing molecules

For the sake of clarity, Figure 13 presents the line intensity profiles of three carbon-bearing molecules along the major axis of the EE and the EDE (i.e., the minor axis of the EE). As shown in the right panels of this figure, larger carbon-bearing molecules are located farther out in the EDE. HC_3N and C_4H exhibits a double-peak profile with the latter lying in the extended region of the EDE, while ^{13}CN shows a single peak. Along the direction of the EE major-axis (the left panels of Figure 13), the intensity profiles of ^{13}CN and HC_3N lines are asymmetric with the peak intensities slightly shifting to the southeast. This can be attributed to the obscuration of the emission from the EE by the inclined front torus (see Figure 15). The asymmetry is more pronounced for ^{13}CN , suggesting that this molecule is located in the innermost region of the EE. C_4H lines exhibit a symmetrical intensity profiles, indicating that they are located predominantly in the outer EDE. The HC_3N line profile appears to fall somewhere in between those of the ^{13}CN and C_4H , and could be decomposed into two components respectively corresponding to the EE and EDE.

The breadths (R) of the spatial distributions of the molecular emission along the EDE diration have a relation of $R(^{13}\text{CN}) < R(\text{HC}_3\text{N}) < R(\text{C}_4\text{H})$. The dipole moments (μ) of the three carbon-bearing molecules follow $\mu(^{13}\text{CN}) < \mu(\text{C}_4\text{H}) < \mu(\text{HC}_3\text{N})$. The HC_3N and C_4H lines have a similar excitation energy that is substantially higher than that of the ^{13}CN lines (Table 1). Therefore, it is hard to explain the different spatial distributions of the molecular emission in the EDE in terms of different excitation conditions, which are more likely to stem from chemistry.

In the gas-phase chemistry, HC_3N is primarily formed through the reaction between C_2H_2 and CN (Agúndez et al. 2017). The gas ejected from the stellar surface is rich in C_2H_2 and HCN. CN is available only when HCN is dissociated by sufficiently intense UV radiation. According to traditional as-

trochemical models, UV photons are mainly from the interstellar medium, and thus CN and HC₃N should be enriched in the outer regions of the envelope with CN lying more outside (see e.g., Millar & Herbst 1994; Agúndez et al. 2017). This is opposite to our observations, providing a strong evidence for the photochemistry driven by the internal UV radiation. The photochemistry of the cyanopolyne family has also been revealed in CRL 618 (Pardo et al. 2005). However, CRL 618 has a central B0 star that has developed a compact ionized region, and thus is now leaving the PPN stage. Unlike that of CRL 618, the central stars of 21 μ m sources have a temperature of ~ 5000 K; their photochemistry may be driven by an obscured hot companion.

There are two potential routes to form circumstellar C₄H. First, this species can be formed via C₂H₂+C₂H, where C₂H can be enriched by the photodissociation of HC₃N (Agúndez et al. 2017). If this is the case, the distribution of C₄H provides a further supporting argument for the hypothesis of an internal photochemistry. Alternatively, C₄H can be formed via C₂H₂+C₂ which is efficient even at low temperatures (Canosa et al. 2007). The outer midplane of the EDE is short of photon heating, and thus is colder, providing a favourable environment for the formation of C₄H. This is consistent with the observed spatial distribution of C₄H. The rate coefficients of these neutral-neutral reactions are typically 10^{-10} cm³ s⁻¹. If assuming the density of C₂H₂ to be 1 cm⁻³, the reaction timescale is ~ 300 years, which is comparable to the dynamical timescale of the EDE. Since large hydrocarbons can be formed in the EDE, it is reasonable to speculate that it also harbours more complex organics. The enhancement of hydrocarbon clusters in 21 μ m sources have been taken as an indication of carbonaceous molecules as the carrier of the 21 μ m feature (Buss et al. 1990).

4.2.2. Silicon-bearing molecules

Differing from carbon-bearing molecules, silicon-bearing molecules are distributed around the periphery of the EDE (Figure 5). Given their refractory nature, silicon-bearing molecules can readily condense onto dust particles. Massalkhi et al. (2018) find that the SiC₂ abundance in carbon-rich AGB envelopes strongly decrease with increasing density, and infer that SiC₂ is the gas-phase precursor of SiC dust. The absence of gaseous silicon-bearing molecules in the EDE may suggest an efficient dust formation. This conforms with the mid-infrared detection of the EDE in IRAS 07134+1005 (Ueta et al. 2000; Kwok et al. 2002). The synthesis of circumstellar SiC₂ has been a long-standing debate, centered on whether it is a parent molecule existing in the photosphere or a daughter species formed in the outer envelope through ion recombination reactions of parent molecules (Howe & Millar 1990; Feng et al. 2023). As shown in Figure 5, SiC₂ and SiS seem to exhibit complementary spatial distributions, suggesting that the two species are chemically linked. SiC₂ can be formed from SiS through the reaction routes SiS \rightarrow SiC₂H⁺ \rightarrow SiC₂.

Notably, a broad emission around 30 μ m is consistently detected in sources exhibiting the 21 μ m feature, suggesting a profound connection between the two features (Volk et al. 2020). The 30 μ m feature is widely attributed to MgS (Goebel & Moseley 1985; Nuth et al. 1985). Zhukovska & Gail (2008) present that in carbon-rich environments MgS can be formed by reactions between Mg and gas-phase sulfur-bearing molecules only when Si is heavily depleted into solid SiC. Otherwise S is primarily locked in SiS. Therefore, the severe condensation of Si-bearing molecules in the EDE may have boosted the formation of MgS. As a results, the 30 μ m feature is strong in this source.

When the dusty EDE is exposed to the internal UV radiation, there may be a wealth of a dust-gas chemistry (Van de Sande et al. 2023). Complex organic molecules, such as hydrogenated fullerenes (Zhang 2020), may be efficiently formed and be responsible for the 21 μ m feature. This hypothesis is consistent with the findings of Kwok et al. (2002) that the aromatic/aliphatic and 21 μ m features and the dust emission arise from the same location.

4.2.3. ¹²CO/¹³CO ratio

It is well established that the isotopic ¹²C/¹³C ratios in evolved stars are lower than the solar value (89). According to Ramstedt & Olofsson (2014), the median values of the ¹²CO/¹³CO abundance ratios in M-, S-, and C-type AGB stars are 13, 26, and 34, respectively. The CN cycle in the hydrogen-burning shell converts ¹²C into the β -unstable isotope ¹³N, which decays into ¹³C. The third dredge-up transports ¹³C to the stellar surface, lowering circumstellar ¹²C/¹³C ratio. In binary stellar systems, the ¹³C enhancement could be caused by nova pollution (Sengupta et al. 2013). The ¹²CO and ¹³CO ($J = 2-1$) lines in IRAS 23304+6147 have an integrated intensity ratio of 7.1. The value is similar to the mean value of other 21 μ m sources (10.3 ± 3.1 , Hrivnak & Bieging 2005; Qiu et al. 2024), suggesting that 21 μ m sources have a low ¹²C/¹³C abundance ratio. Such low ¹²CO/¹³CO ratios have also been found in binary post-AGB stars with (sub-)Keplerian rotating disks (~ 8.6 , Gallardo Cava et al. 2022). J-type carbon stars have relatively low ¹²C/¹³C ratios which might be related to their binary nature (e.g., Izzard et al. 2007; Sengupta et al. 2013; Abia & Isern 2000), although the exact cause is unclear. It is reasonable to hypothesize that the 21 μ m sources might be descended from J-type carbon stars.

Figure 14 presents the ¹²CO/¹³CO map, demonstrating the notable differences between the EDE and EE. The ratio is comparatively low (6.9–15) in the EDE and larger (20–50) in the EE, peaking in the outermost regions. This might be because the EDE's optical thickness is higher than the EE's. On the other hand, the outermost regions of the EE are exposed to the interstellar radiation field, causing photodissociation of ¹³CO. As ¹²CO may remain largely intact due to its self-shielding effect, the ¹²CO/¹³CO is larger in the tips of the EE. As shown in Figure 5, the ¹²CO emission has a larger extent along the EE major axis than the ¹³CO emission. Therefore, ¹³CO is unable to fully represent the actual nebular structure. We propose that the EE and EDE may constitute structural components of an oval-shaped nebula. In Figure 15, we present a schematic illustration of the intrinsic geometry of this PPN, with the diffuse halo omitted for visual clarity.

5. Conclusion

We present interferometric NOEMA maps of gas-phase molecules in the 21 μ m source IRAS 23304+6147, which offer valuable information about the structure of this nebula. Eight different molecules and isotopologues are observed, among which six (C¹⁸O, SiS, SiC₄, ¹³CN, HC₃N, and C₄N) are new detections in this object. In comparison to the extensive research on the chemistry of AGB envelopes, the chemistry of PPNe has been barely explored. The newly detected molecular lines have, to some extent, deepened our understanding of the molecular chemistry in these objects. We constructed a morpho-kinematic model to reproduce the observed maps. A chemically stratified structure is revealed, showcasing two distinct features: EDE and EE. Based on the ¹³CO emission, we estimate that the nebular

mass is larger than $1.3 \times 10^{-2} M_{\odot}$. A comparison with single-dish observations indicates that an extended halo might be missed by our interferometric observations. Linear carbon-chain molecules preferentially distribute in the EDE, forming a torus-like structure. The different spatial distributions of ^{13}CN , HC_3N , and C_4H provide a strong evidence that the internal UV radiation initiates the photochemistry. SiS and SiC_2 maps exhibit a hollow, indicating to an efficient dust formation in the EDE. These results show that the transition of the PPN morphology may result in significant chemical differentiation. As a result, different species may have distinct spatial distributions, and the morphokinematics of PPNs have a molecule dependence.

The $^{12}\text{CO}/^{13}\text{CO}$ ratios span from 6.9 in the core of the EDE to 50 in the tips of EE and stay approximately constant in the main nebular regions. This suggests that the EDE is optically thick in ^{12}CO and that ^{13}CO has been significantly photodissociated in the outermost regions. The generally low $^{12}\text{CO}/^{13}\text{CO}$ ratio and the presence of EDE structure in IRAS 23304+6147 seem to indicate that its progenitor is probably a J-type carbon star within a binary system.

Such a carbon-rich EDE may hold the vital clue to the origin of the $21 \mu\text{m}$ feature. Our observations show that the EDE serves as a favourable environment for dust formation and molecular synthesis. Speculatively, complex aromatic/aliphatic compounds can be formed in the EDE, some of which, such as hydrogenated fullerenes, might be the carrier of the $21 \mu\text{m}$ feature.

Acknowledgements. We thank the anonymous reviewer for insightful suggestions, which have significantly improved the quality of this work. We are grateful to Ana Lopez Sepulcre and Michael Bremer for their helps in the data reduction. The financial supports of this work are from the National Natural Science Foundation of China (NSFC, No. 12473027, 12333005, and 11973099), the Guangdong Basic and Applied Basic Research Funding (No. 2024A1515010798), and the science research grants from the China Manned Space Project (NO. CMS-CSST-2021-A09, CMS-CSST-2021-A10, etc). Y.Z. thanks the Xinjiang Tianchi Talent Program (2023). X.H.L. acknowledges support from the Natural Science Foundation of Xinjiang Uygur Autonomous Region (No. 2024D01E37) and the National Science Foundation of China (12473025). This work is based on observations carried out with the IRAM NOEMA Interferometer. IRAM is supported by INSU/CNRS (France), MPG (Germany) and IGN (Spain).

References

- Abia, C. & Isern, J. 2000, *ApJ*, 536, 438
 Agúndez, M., Cernicharo, J., Quintana-Lacaci, G., et al. 2017, *A&A*, 601, A4
 Bloeker, T. 1995, *A&A*, 299, 755
 Boffin, H. M. J., Miszalski, B., Rauch, T., et al. 2012, *Science*, 338, 773
 Bollen, D., Kamath, D., Van Winckel, H., et al. 2022, *A&A*, 666, A40
 Bujarrabal, V., Alcolea, J., & Planesas, P. 1992, *A&A*, 257, 701
 Bujarrabal, V., Castro-Carrizo, A., Alcolea, J., et al. 2016, *A&A*, 593, A92
 Bujarrabal, V., Castro-Carrizo, A., Alcolea, J., & Van Winckel, H. 2015, *A&A*, 575, L7
 Bujarrabal, V., Castro-Carrizo, A., Alcolea, J., et al. 2013, *A&A*, 557, L11
 Bujarrabal, V., Castro-Carrizo, A., Van Winckel, H., et al. 2018, *A&A*, 614, A58
 Buss, R. H. J., Cohen, M., Tielens, A. G. G. M., et al. 1990, *ApJ*, 365, L23
 Canosa, A., Páramo, A., Le Picard, S. D., & Sims, I. R. 2007, *Icarus*, 187, 558
 Cernicharo, J., Guélin, M., & Kahane, C. 2000, *A&AS*, 142, 181
 Chen, P.-S., Yang, X.-H., & Zhang, P. 2007, *AJ*, 134, 214
 Chiu, P.-J., Hoang, C.-T., Dinh-V-Trung, et al. 2006, *ApJ*, 645, 605
 De Nutter, R., Decin, L., Olofsson, H., et al. 2017, *A&A*, 600, A71
 Decin, L. 2021, *ARA&A*, 59, 337
 Decin, L., Homan, W., Danilovich, T., et al. 2019, *Nature Astronomy*, 3, 408
 Decin, L., Montargès, M., Richards, A. M. S., et al. 2020, *Science*, 369, 1497
 Dinh-V-Trung, 2009, *ApJ*, 692, 1382
 Engels, D. 1979, *A&AS*, 36, 337
 Feng, Y., Li, X., Millar, T. J., et al. 2023, *Frontiers in Astronomy and Space Sciences*, 10, 1215642
 Gallardo Cava, I. 2023, arXiv e-prints, arXiv:2311.08034
 Gallardo Cava, I., Bujarrabal, V., Alcolea, J., Gómez-Garrido, M., & Santander-García, M. 2022, *A&A*, 659, A134
 Gallardo Cava, I., Gómez-Garrido, M., Bujarrabal, V., et al. 2021, *A&A*, 648, A93
 Goebel, J. H. & Moseley, S. H. 1985, *ApJ*, 290, L35
 Högbom, J. A. 1974, *A&AS*, 15, 417
 Howe, D. A. & Millar, T. J. 1990, *MNRAS*, 244, 444
 Hrivnak, B. J. & Bieging, J. H. 2005, *ApJ*, 624, 331
 Izzard, R. G., Jeffery, C. S., & Lattanzio, J. 2007, *A&A*, 470, 661
 Jiang, B. W., Zhang, K., & Li, A. 2010, *Earth, Planets, and Space*, 62, 105
 Kamath, D., Van Winckel, H., Ventura, P., et al. 2022, *ApJ*, 927, L13
 Klochkova, V. G., Szczerba, R., & Panchuk, V. E. 2000, *AstL*, 26, 88
 Koning, N., Kwok, S., & Steffen, W. 2011, *ApJ*, 740, 27
 Kwok, S., Volk, K., & Bernath, P. 2001, *ApJ*, 554, L87
 Kwok, S., Volk, K., & Hrivnak, B. J. 2002, *ApJ*, 573, 720
 Kwok, S., Volk, K. M., & Hrivnak, B. J. 1989, *ApJ*, 345, L51
 Lagadec, E. 2018, *Galaxies*, 6, 99
 Likkel, L., Forveille, T., Omont, A., & Morris, M. 1991, *A&A*, 246, 153
 Masa, E., Alcolea, J., Santander-García, M., et al. 2024, *Galaxies*, 12, 63
 Massalkhi, S., Agúndez, M., Cernicharo, J., et al. 2018, *A&A*, 611, A29
 Millar, T. J. 2020, *Chinese Journal of Chemical Physics*, 33, 668
 Millar, T. J. & Herbst, E. 1994, *A&A*, 288, 561
 Nakashima, J.-i., Koning, N., Kwok, S., & Zhang, Y. 2009, *ApJ*, 692, 402
 Nakashima, J.-i., Koning, N., Volgenau, N. H., et al. 2012, *ApJ*, 759, 61
 Nuth, J. A., Moseley, S. H., Silverberg, R. F., Goebel, J. H., & Moore, W. J. 1985, *ApJ*, 290, L41
 Olofsson, H., Eriksson, K., Gustafsson, B., & Carlstrom, U. 1993, *ApJS*, 87, 267
 Olofsson, H. & Nyman, L. Å. 1999, *A&A*, 347, 194
 Omont, A., Loup, C., Forveille, T., et al. 1993, *A&A*, 267, 515
 Pardo, J. R., Cernicharo, J., & Goicoechea, J. R. 2005, *ApJ*, 628, 275
 Pardo, J. R., Cernicharo, J., Goicoechea, J. R., Guélin, M., & Asensio Ramos, A. 2007, *ApJ*, 661, 250
 Park, J. A., Cho, S.-H., Lee, C. W., & Yang, J. 2008, *AJ*, 136, 2350
 Qiu, J.-J., Zhang, Y., Nakashima, J.-i., et al. 2024, *AJ*, 167, 91
 Qiu, J.-J., Zhang, Y., Zhang, J.-S., & Nakashima, J.-i. 2022, *ApJS*, 259, 56
 Ramstedt, S. & Olofsson, H. 2014, *A&A*, 566, A145
 Sahai, R., Morris, M., Sánchez Contreras, C., & Claussen, M. 2007, *AJ*, 134, 2200
 Sahai, R. & Trauger, J. T. 1998, *AJ*, 116, 1357
 Sahai, R., Vlemmings, W. H. T., Gledhill, T., et al. 2017, *ApJ*, 835, L13
 Sánchez Contreras, C., Bujarrabal, V., Castro-Carrizo, A., Alcolea, J., & Sargent, A. 2004, *ApJ*, 617, 1142
 Sánchez Contreras, C. & Sahai, R. 2012, *ApJS*, 203, 16
 Santander-García, M., Bujarrabal, V., Koning, N., & Steffen, W. 2015, *A&A*, 573, A56
 Sengupta, S., Izzard, R. G., & Lau, H. H. B. 2013, *A&A*, 559, A66
 Steffen, W. & Koning, N. 2012, *Shape: A 3D Modeling Tool for Astrophysics*, *Astrophysics Source Code Library*, record ascl:1204.010
 Tafuya, D., Orosz, G., Vlemmings, W. H. T., Sahai, R., & Pérez-Sánchez, A. F. 2019, *A&A*, 629, A8
 Ueta, T., Izumiura, H., Yamamura, I., & Otsuka, M. 2019, in *Why Galaxies Care About AGB Stars: A Continuing Challenge through Cosmic Time*, ed. F. Kerschbaum, M. Groenewegen, & H. Olofsson, Vol. 343, 520–521
 Ueta, T., Meixner, M., & Bobrowsky, M. 2000, *ApJ*, 528, 861
 Van de Sande, M., Walsh, C., & Millar, T. J. 2023, *Faraday Discussions*, 245, 586
 van der Tak, F. F. S., Black, J. H., Schöier, F. L., Jansen, D. J., & van Dishoeck, E. F. 2007, *A&A*, 468, 627
 van Winckel, H. 2003, *ARA&A*, 41, 391
 Vassiliadis, E. & Wood, P. R. 1993, *ApJ*, 413, 641
 Volk, K., Sloan, G. C., & Kraemer, K. E. 2020, *Ap&SS*, 365, 88
 Woodsworth, A. W., Kwok, S., & Chan, S. J. 1990, *A&A*, 228, 503
 Zhang, K., Jiang, B. W., & Li, A. 2009, *MNRAS*, 396, 1247
 Zhang, Y. 2020, *ApJ*, 898, 151
 Zhang, Y. & Kwok, S. 2011, *ApJ*, 730, 126
 Zhang, Y., Kwok, S., & Hrivnak, B. J. 2010, *ApJ*, 725, 990
 Zhang, Y., Kwok, S., Nakashima, J.-i., Chau, W., & Dinh-V-Trung. 2013, *ApJ*, 773, 71
 Zhukovska, S. & Gail, H. P. 2008, *A&A*, 486, 229

Table 1. Molecular lines detected in the observations.

Molecule	Transition	E_u (K)	Frequency (MHz)	I_{peak} (K)	$\int I dv$ (K km s ⁻¹)	rms (K)
CO	J=2-1	16.59	230538.00	22.17	216.80	0.16
¹³ CO	J=2-1	15.86	220398.67	3.14	30.65	0.14
HC ₃ N	J=24-23	130.98	218324.71	2.03	18.85	0.14
SiC ₂	$J_{Ka,Kc} = 9_{4,6} - 8_{4,5}$	82.28	213208.03	0.32	2.04	0.15
	$J_{Ka,Kc} = 9_{4,5} - 8_{4,4}$	82.28	213292.33	0.32	2.01	0.15
	$J_{Ka,Kc} = 10_{2,9} - 9_{2,8}$	69.62	232534.07	0.28	1.97	0.18
	$J_{Ka,Kc} = 10_{6,5} - 9_{6,4}$	132.37	235713.00	0.25	1.85	0.18
C ₄ H	N,J=23-22, 47/2-45/2	126.03	218836.98	0.38	3.15	0.14
	N,J=23-22, 45/2-43/2	126.07	218875.35	0.45	3.56	0.14
	N,J=24-23, 47/2-45/2	137.03	228386.92	0.40	3.11	0.16
C ¹⁸ O	J=2-1	15.81	219560.35	0.32	2.81	0.14
SiS	J=12-11	67.95	217817.66	0.18	0.58	0.14
¹³ CN	N,J,F=2-1,3/2-1/2,2-2	15.66	217074.23	0.15	...	0.14
	N,J,F=2-1,5/2-3/2,3-2	15.65	217303.19	0.71	...	0.14
	N,J,F=2-1,3/2-1/2,2-1	15.66	217304.92	0.72	5.12	0.14
	N,J,F=2-1,5/2-3/2,2-2	15.68	217437.70	0.38	2.10	0.14
	N,J,F=2-1,5/2-3/2,4-3	15.68	217467.15	0.52	...	0.14
	N,J,F=2-1,5/2-3/2,2-1	15.69	217469.15	0.52	4.10	0.14
	N,J,F=2-1,5/2-1/2,2-1	15.68	217668.43	0.17	1.13	0.14
	N,J,F=2-1,5/2-1/2,1-1	15.68	217675.39	0.17	1.11	0.14

Notes. The coefficient to convert the intensity unit from Jy beam⁻¹ to K is 105–122 K/(Jy beam⁻¹) at 100–122 GHz for a synthesized beam size of 0.52'' × 0.42''.

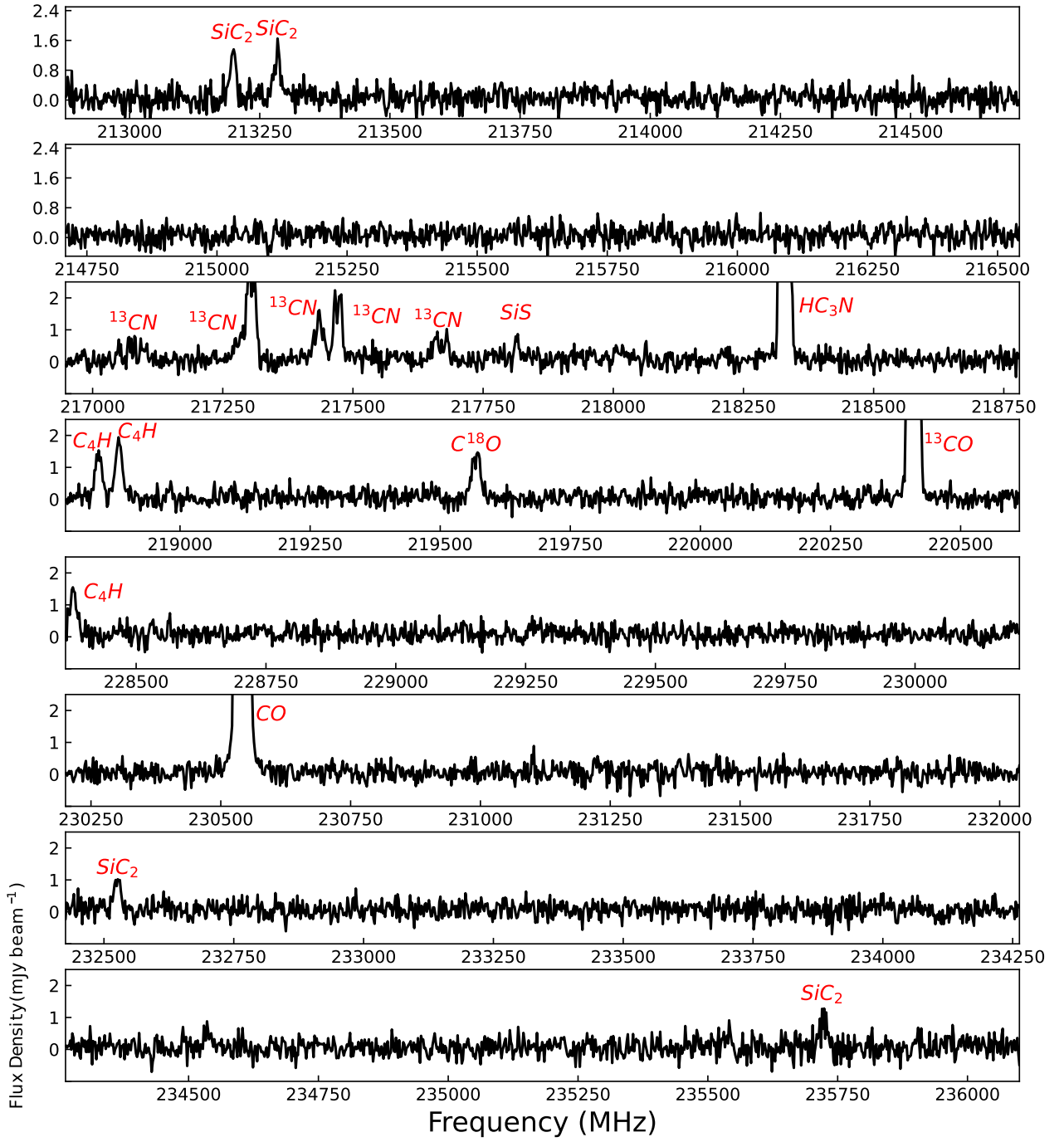


Fig. 1. NOEMA spectra of IRAS 23304+6147 in the frequency ranges of 213–221 GHz (LSB) and 228–236 GHz (USB).

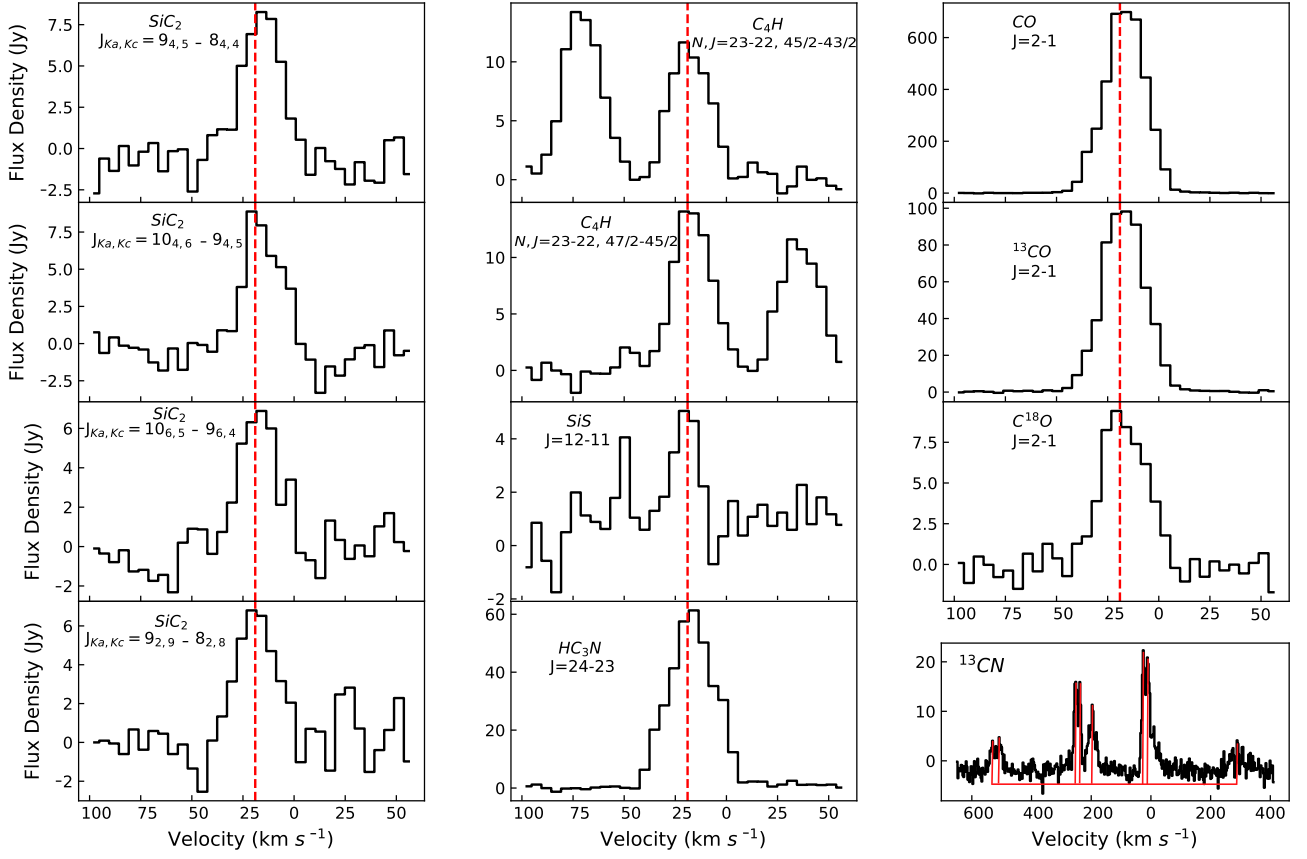


Fig. 2. Profiles of the lines detected in IRAS 23304+6147. The systemic velocity (-16.1 km s^{-1}) is indicated by the vertical dashed line. The positions and relative intensities of the hyperfine components of ^{13}CN are marked by vertical solid lines.

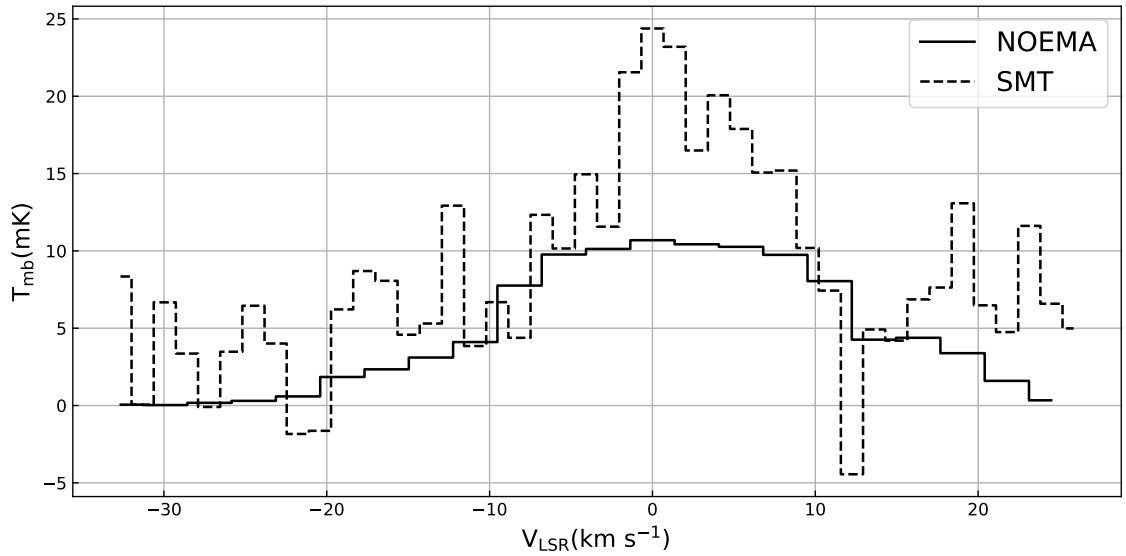


Fig. 3. Comparison of the $^{13}\text{CO } J = 2-1$ observations made by NOEMA and SMT. The NOEMA data have been convolved to match the SMT's resolution of $34.3''$. The central velocity is set to 0 km s^{-1} .

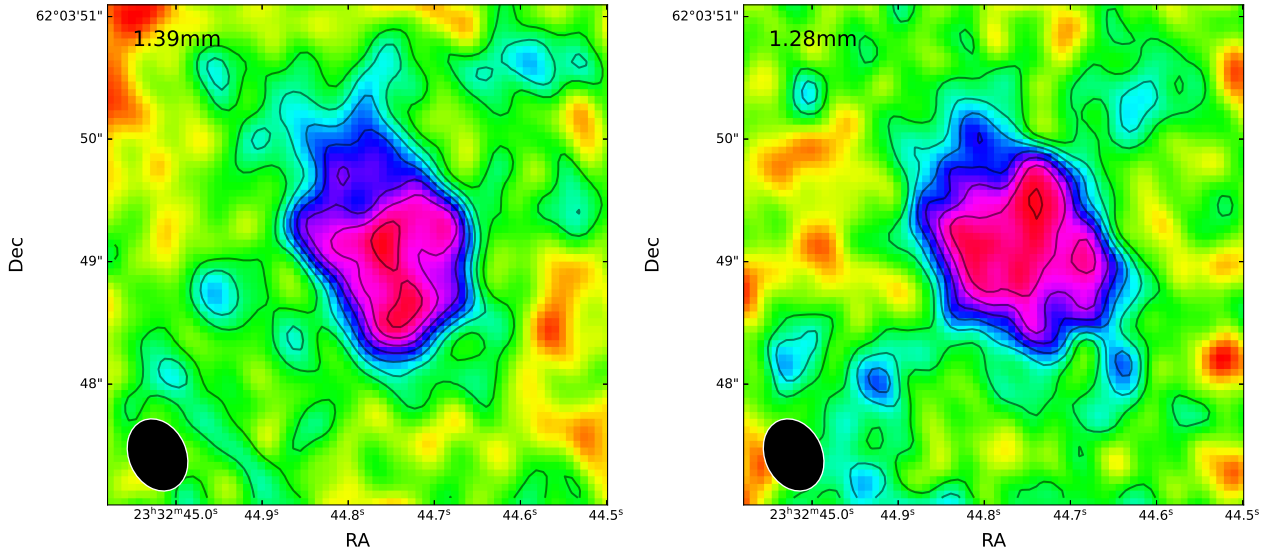


Fig. 4. Continuum emission at 1.39 and 1.28 mm wavelengths. The synthesized beams shown in the down-left corner are of size $0.52'' \times 0.42''$. Contour levels are at 1σ intervals starting at 1σ , where the rms $\sigma = 41$ and $55 \mu\text{Jy beam}^{-1}$ at 1.39 and 1.28 mm, respectively.

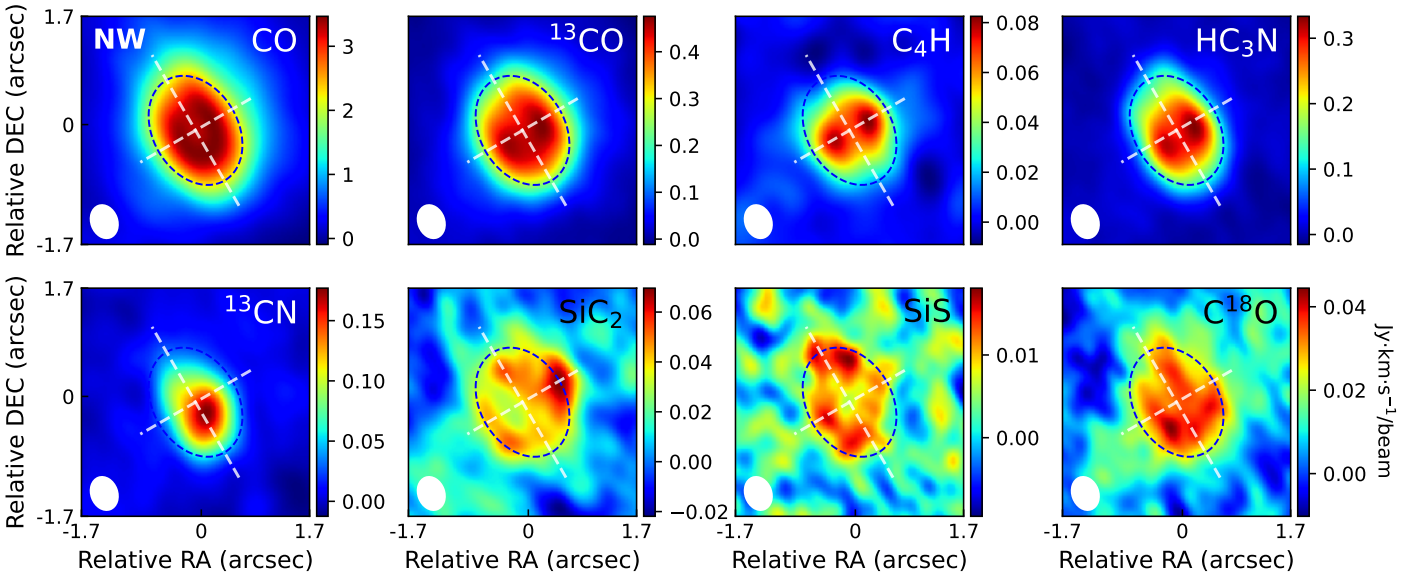


Fig. 5. Integrated intensity (moment 0) maps of the molecular lines detected in IRAS 23304+6147. The white ellipse at the down-left corner represents the synthesized beam. For comparison convenience, in each panel the dashed elliptical circles indicate the main CO emission region that have a semi-major (PA= 30°) and minor axis (PA= 60°) of $1.16''$ and $0.84''$, and the dashed straight lines mark the size of the extended CO halo. The northwest (NW) direction is marked in the upper-left corner of the CO map.

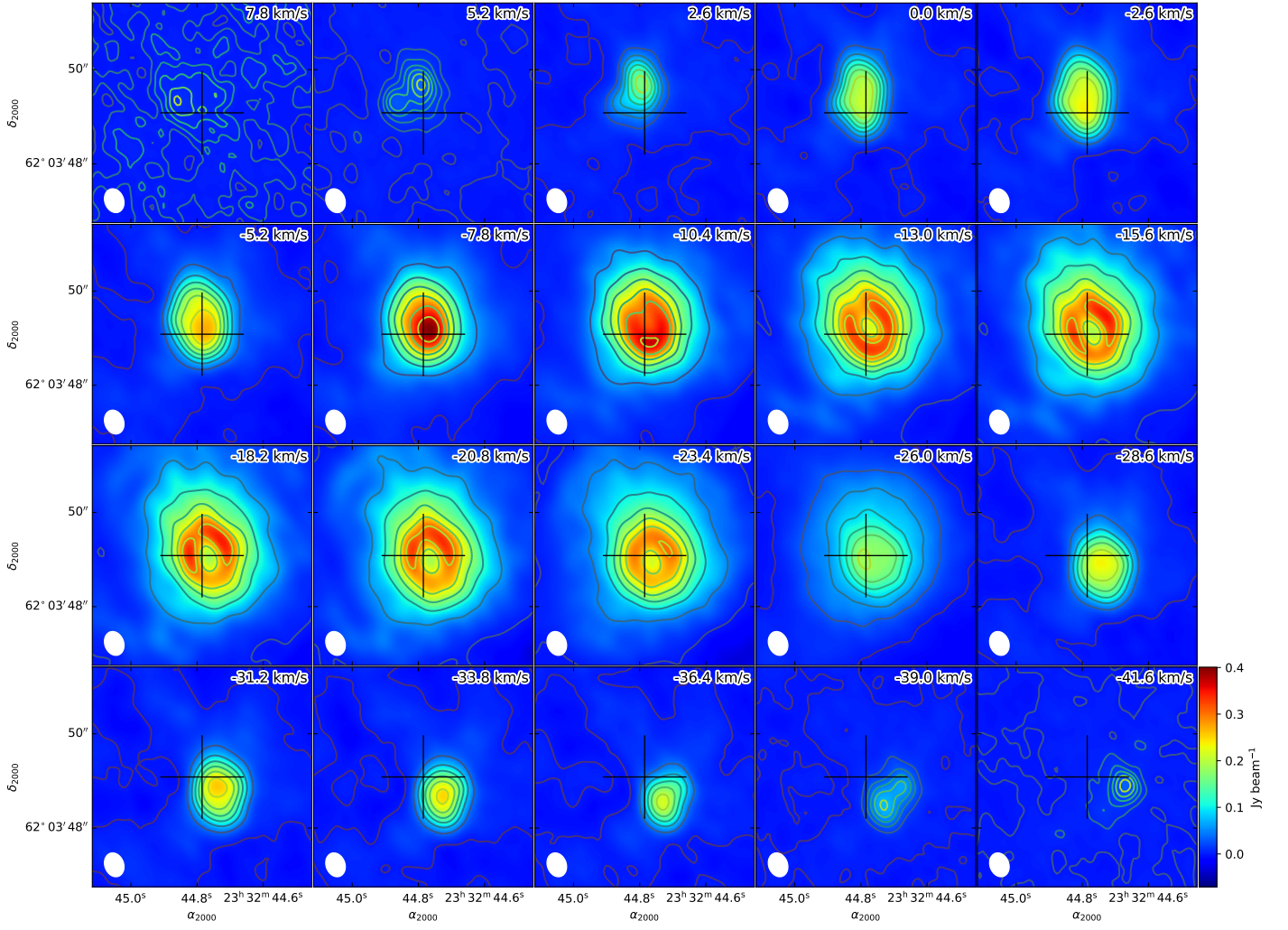


Fig. 6. Channel maps of IRAS 23304+6147 in CO $J = 2 - 1$ emission. The contour levels are individually set for each channel by creating ten equally spaced contour lines between the maximum and minimum intensities of that channel. The crosses mark the position of the phase center. The LSR velocities are indicated in each panel. The systemic velocity of this object is -16.1 km s^{-1} . The white ellipse at the bottom-left corner represents the synthesized beam, with a size of $0.52'' \times 0.42''$ and a PA of 23° .

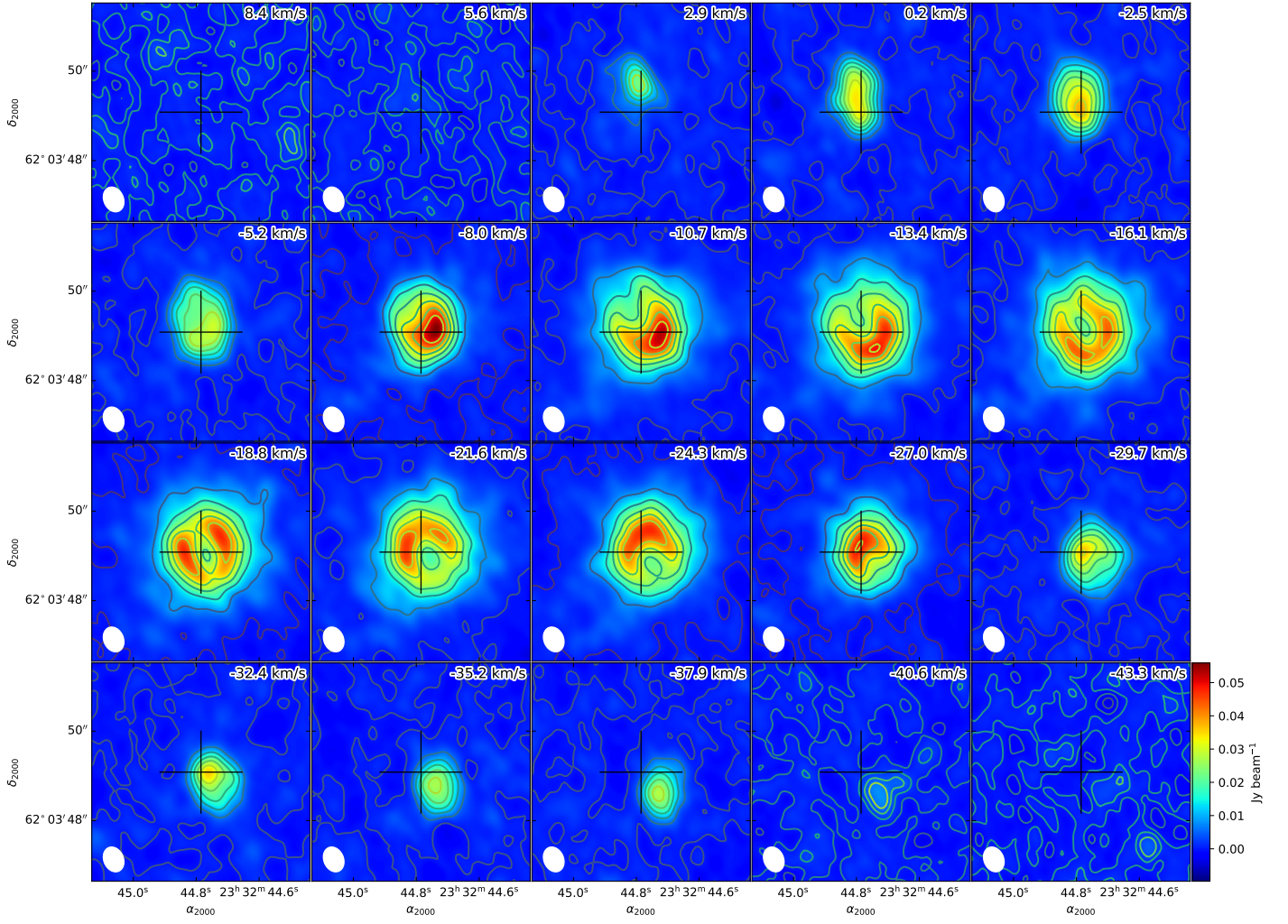


Fig. 7. Same as in Figure 6 but for $^{13}\text{CO } J=2-1$.

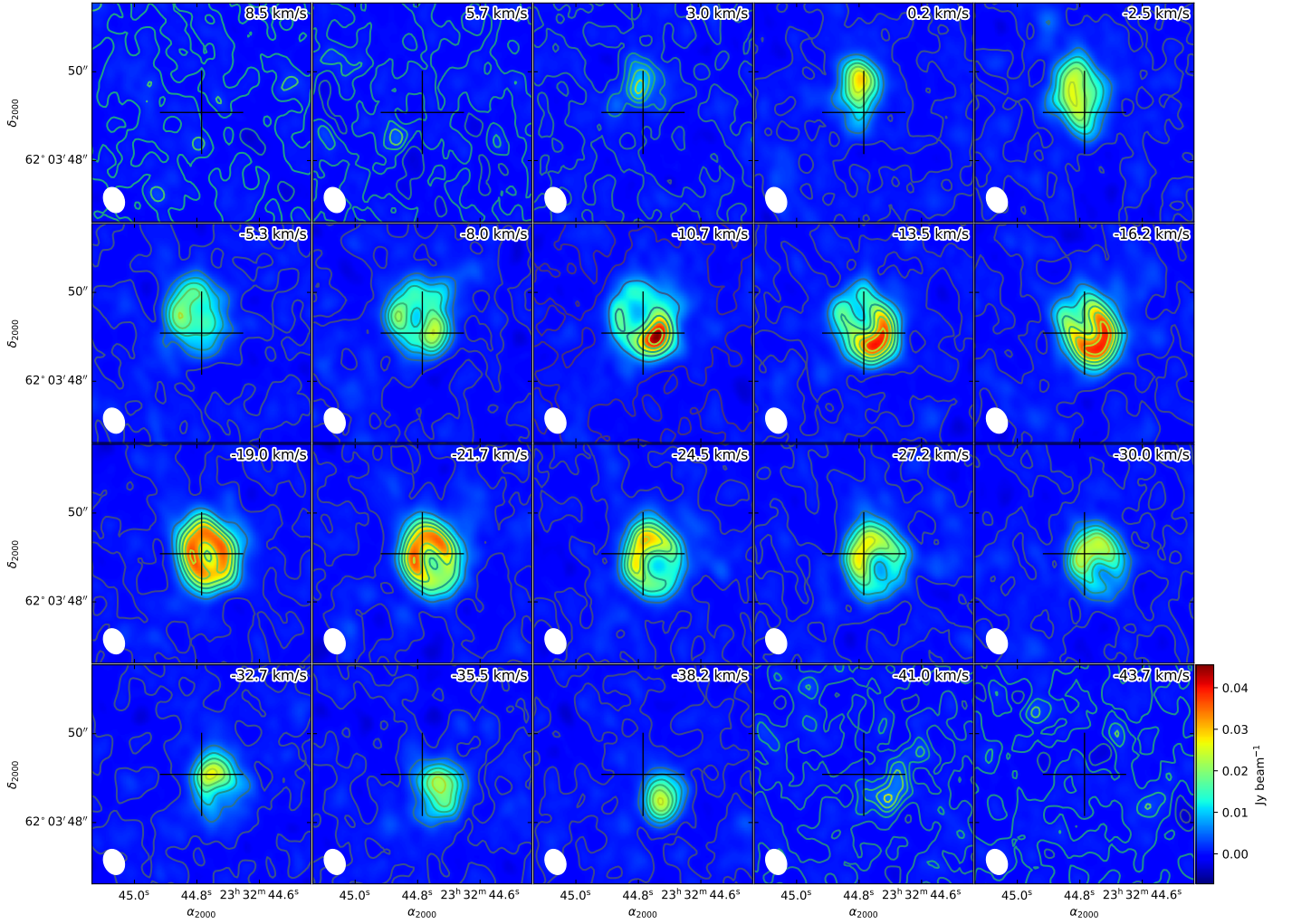


Fig. 8. Same as in Figure 6 but for $\text{HC}_3\text{N } J = 24 - 23$.

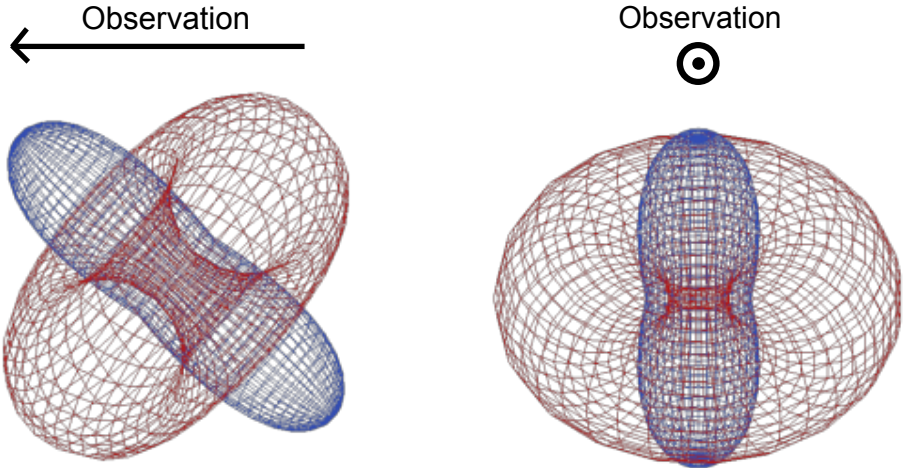


Fig. 9. Three-dimensional mesh geometry of the SHAPE model, as seen from two orthogonal directions. The left panel shows the side view along the observer's direction, while the right panel shows the front view facing the observer. The red torus represents the EDE, and the blue peanut-shaped structure represents the EE. The inner and outer radii of the EDE are assumed to be 0.78 and 1.75'', respectively. The major axis size of the EE is assumed to be 2''.

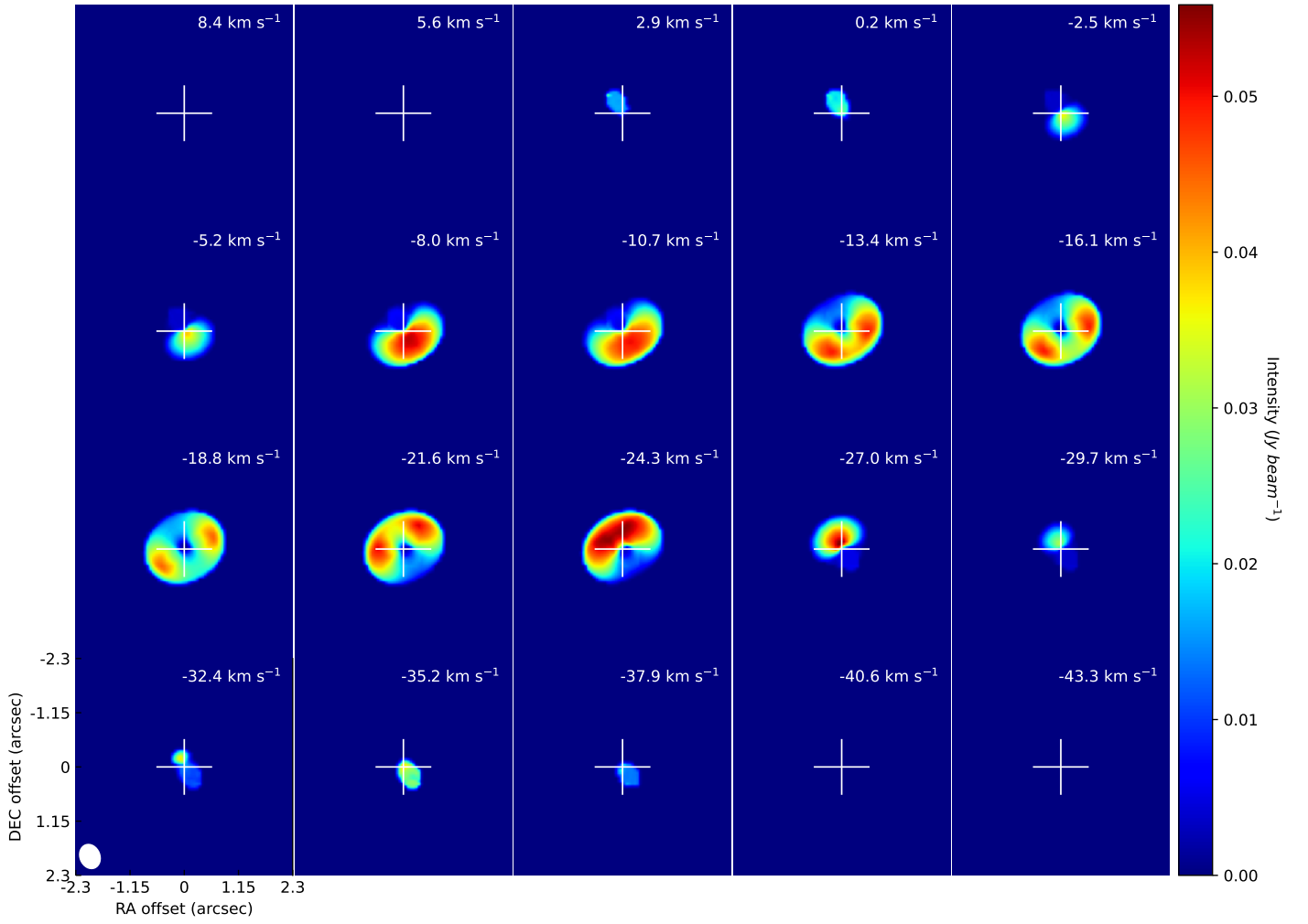


Fig. 10. Modeled ^{13}CO ($J = 2-1$) channel maps. The white ellipse in the lower-left corner of the image represents the synthesized beam. The angular size of each panel is identical to those in Figures 6–8.

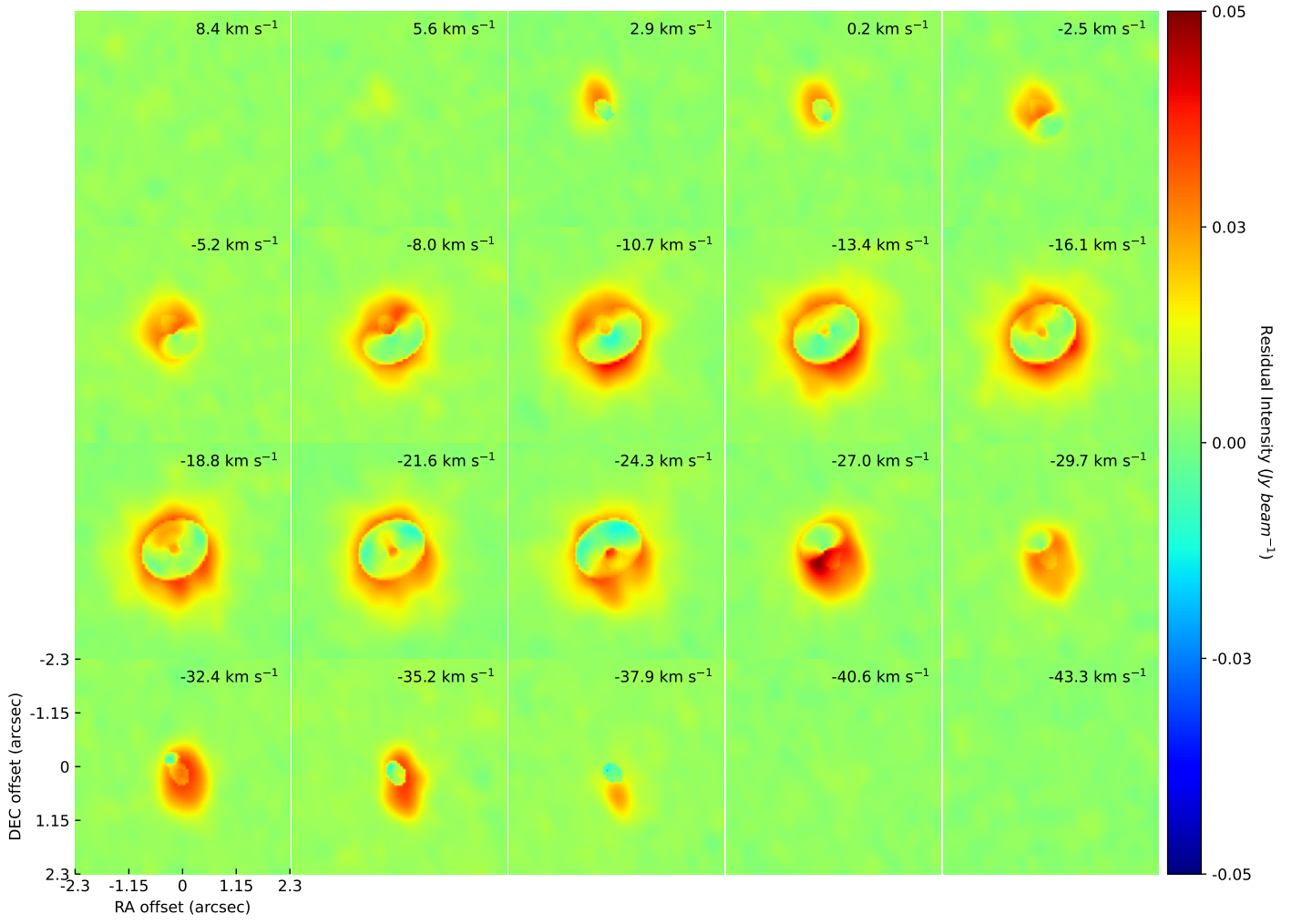


Fig. 11. Residuals between the observed and modeled ^{13}CO ($J = 2-1$) channel maps. The angular size of each panel is identical to those in Figures 6–8.

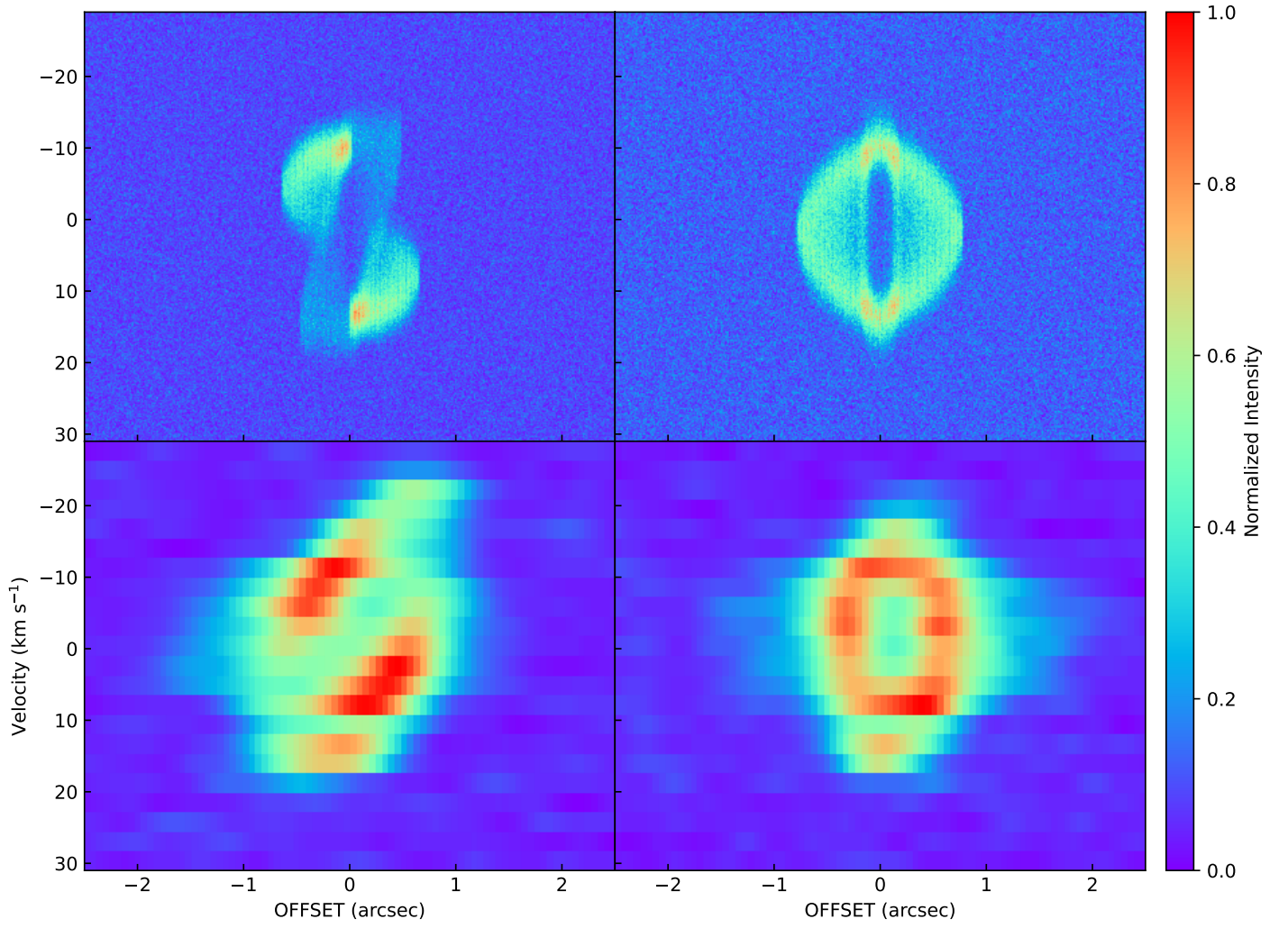


Fig. 12. PV diagrams of the $^{13}\text{CO } J = 2-1$ transition, derived from the modelling (upper panels) and observations (lower panels). The left panels present the velocity structure along the major axis of the EE, oriented from northwest to southeast, where negative offsets indicate the northwest direction. The right panels show the velocity structure along the minor axis, oriented from southwest to northeast, with negative offsets corresponding to the southwest direction. The cuts used to extract these diagrams are detailed in Figure 5.

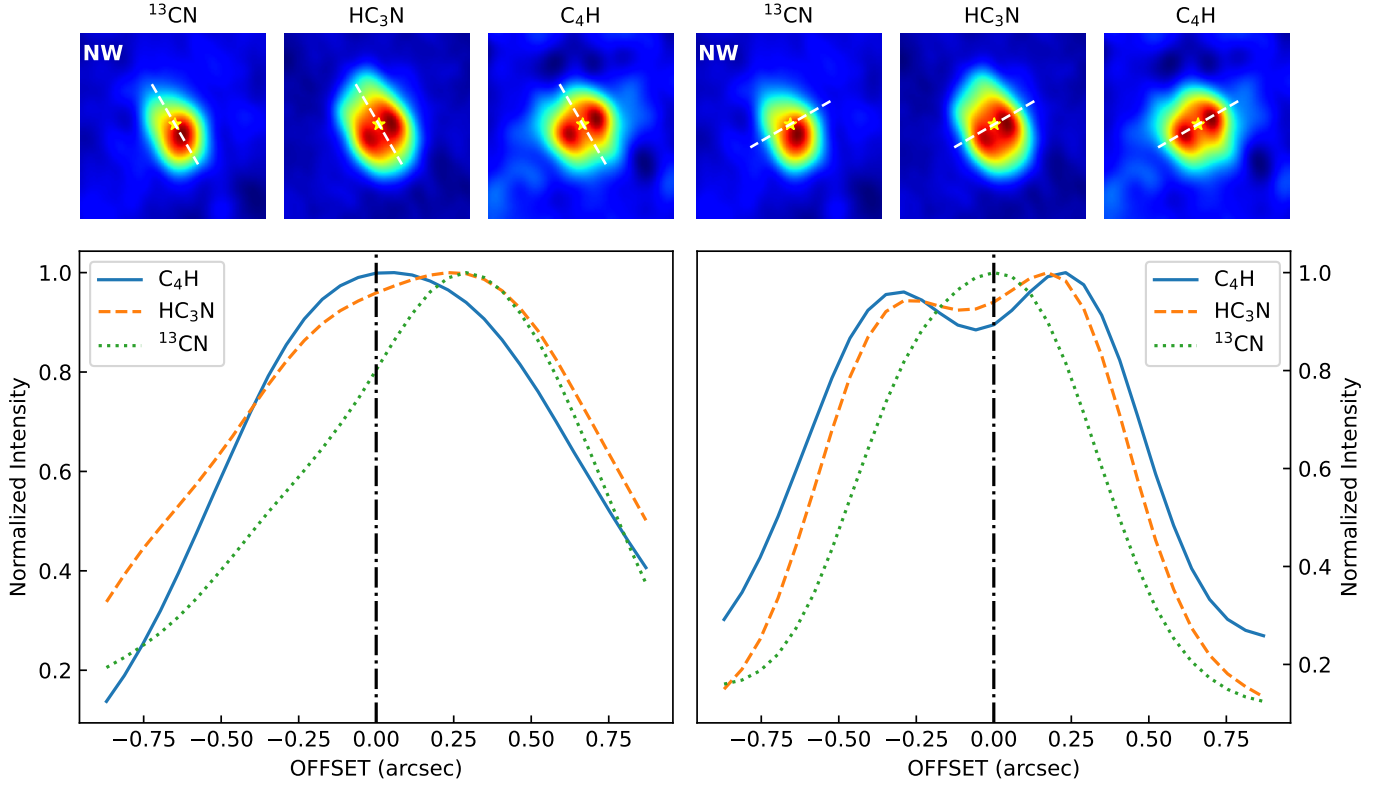


Fig. 13. Spatial distributions of ^{13}CN , HC_3N , and C_4H molecules. The northwest direction is marked in the upper left corner of the ^{13}CN map. The left panels show the molecular line intensity distributions along the major-axis direction, tracking a path from northwest to southeast (with the offset changing from negative to positive) at a PA of 30° relative to the north-south direction. The right panels show the molecular line intensity distributions along the minor-axis direction, tracking a path from southwest to northeast (with the offset changing from negative to positive) at a PA of 60° . In the upper panels, the dashed lines denote the paths along which the line intensity profiles are extracted. The positions of the phase centers are denoted by the pentagrams in the upper panels and the vertical dashed lines in the lower panels.

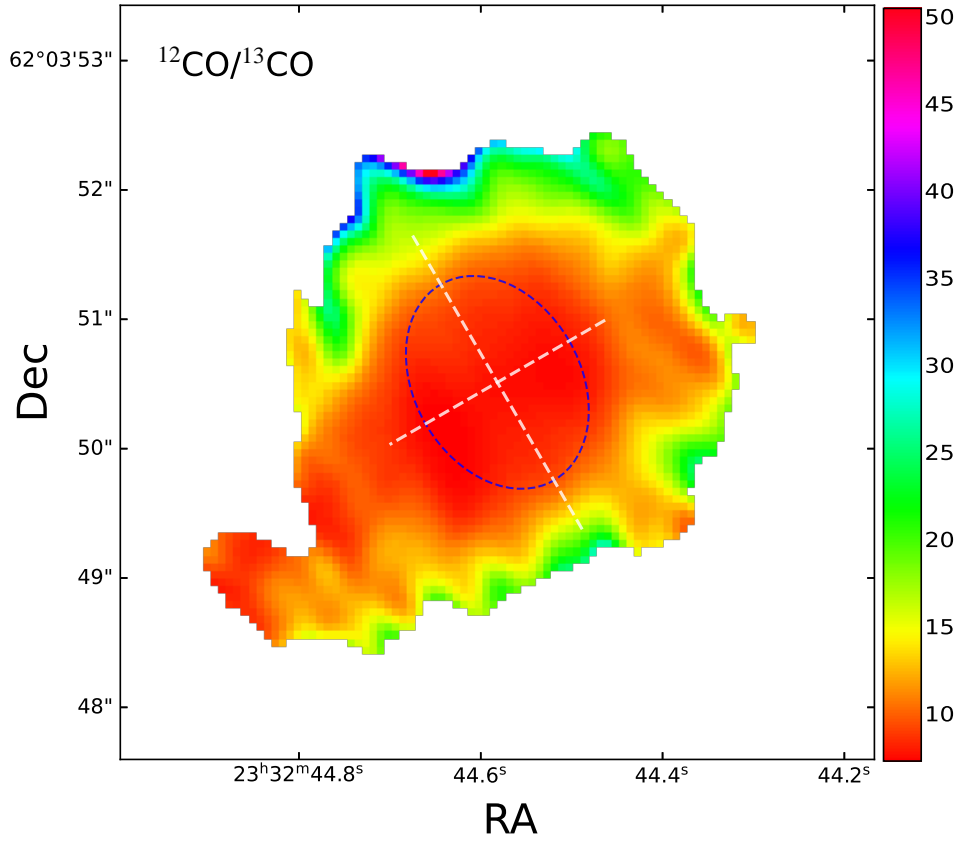


Fig. 14. Ratio map between ^{12}CO and ^{13}CO integrated intensities. The dashed ellipse is the same as that in Figure 5. The major and minor axes of the ellipse align with the EE and EDE direction, respectively.

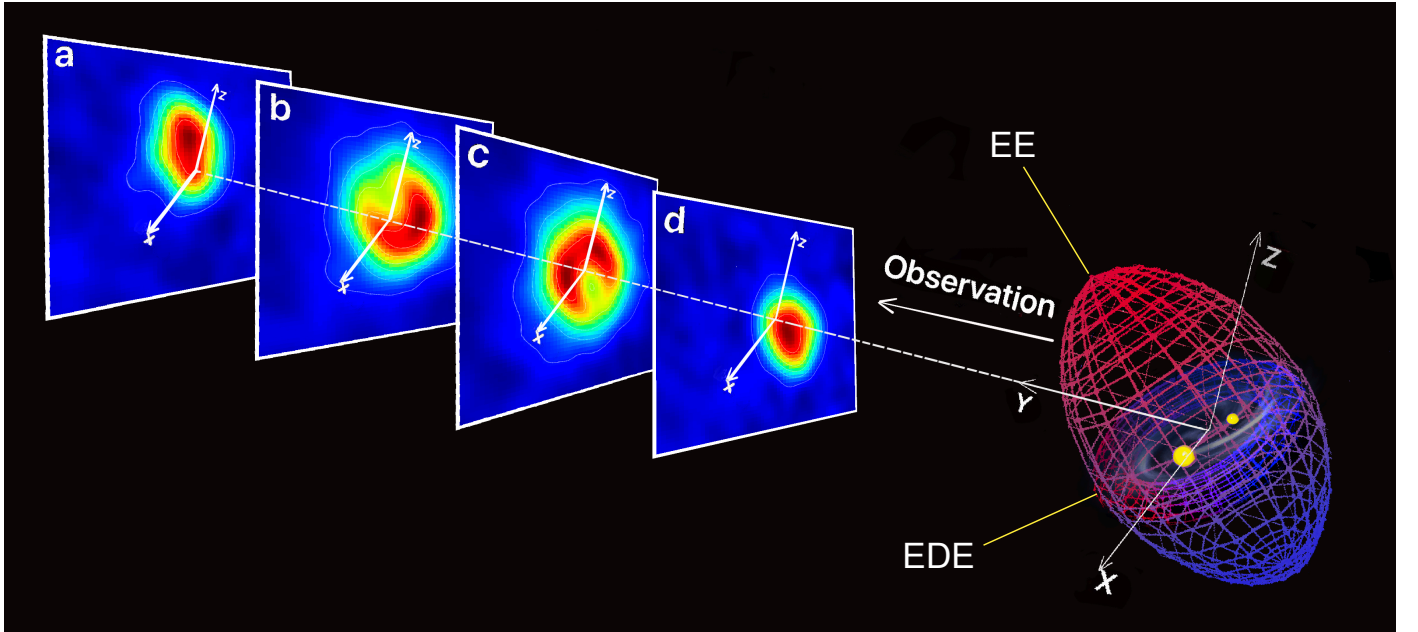


Fig. 15. Schematic illustration of the true shape of IRAS 23304+6147. The grid on the right represents the conceptual model consisting of a hypothetical binary star system (yellow filled circles), an EE, and an EDE. The coloration of the grid is defined according to the Doppler effect, that is, the regions moving away from the observer's perspective (along the Y-axis, as denoted by the arrow below 'Observation') are indicated in red, while those moving towards the observer in blue. Four representational velocity slices are shown on the left: a ($V_{\text{LSR}} = -3$ to 3 km s^{-1}), b ($V_{\text{LSR}} = -16$ to -5 km s^{-1}), c ($V_{\text{LSR}} = -27$ to -18 km s^{-1}), and d ($V_{\text{LSR}} = -40$ to -29 km s^{-1}). The nebula is projected onto the X-Z plane (the sky plane). From the observer's perspective, from the far to near sides, the EE is first seen in channel 'a' and progresses towards 'd', while the EDE shifts from channel 'b' to 'c'.